International Journal of Nanomedicine

Dovepress
Taylor & Francis Group

Open Access Full Text Article

ORIGINAL RESEARCH

Preparation of Fe_2O_3/GCN/ICG/DHA Nanocomplexes and Their Multifunctional Combined Antitumor Properties

Junyu Liu[1,*], Li Zhang[2,*], Xiaoyu Zhou[1], Yingge Yue[1], Wenjin He[2], Keming Yun[3], Xiangyu Wang[1], Wei Bian[2]

[1]Shanxi Province Key Laboratory of Oral Diseases Prevention and New Materials, Shanxi Medical University School and Hospital of Stomatology, Taiyuan, Shanxi, People's Republic of China; [2]School of Basic Medical Science, Shanxi Medical University, Taiyuan, Shanxi, People's Republic of China; [3]School of Forensic Medicine, Shanxi Medical University, Taiyuan, Shanxi, People's Republic of China

*These authors contributed equally to this work

Correspondence: Xiangyu Wang, Shanxi Province Key Laboratory of Oral Diseases Prevention and New Materials, Shanxi Medical University School and Hospital of Stomatology, Taiyuan, Shanxi, 030000, People's Republic of China, Email wangxiangyu76@163.com; Wei Bian, School of Basic Medical Science, Shanxi Medical University, Taiyuan, Shanxi, 030000, People's Republic of China, Email weibian@sxmu.edu.cn

Introduction: Malignant tumors seriously affect people's normal lives, but the effective treatment of cancer needs to be further improved.
Methods: In this study, we prepared nanocomposites with photothermal therapy (PTT)/photodynamic therapy (PDT)/chemodynamic therapy (CDT) properties named Fe_2O_3/GCN/ICG/DHA. Under high H_2O_2 conditions, Fe^{3+} is reduced to Fe^{2+} and reacts with DHA to produce C-center free radicals, which kill tumor cells. In addition, ICG produced a warming effect and cytotoxic singlet oxygen with 808 nm laser irradiation.
Results: The significant combined antitumor activity of Fe_2O_3/GCN/ICG/DHA, validated in vitro and in vivo, provides strong experimental support for advancing this transition metal iron-based nanocomplex towards tumor therapy applications.
Discussion: It expands the potential applications of novel nanocomplex in the field of tumor therapy.
Keywords: nanocomplexes, malignant tumors, chemodynamic therapy, photothermal therapy, photodynamic therapy

Introduction

Cancer poses a major challenge to global public health and a serious threat to human health and life.[1,2] There are three main types of treatments: surgery, radiotherapy, and chemotherapy (CT).[3] Although these therapies can inhibit tumor growth to a certain extent, they are accompanied by a series of side effects and complications that limit their application.[4–6] New therapeutic approaches such as phototherapy, immunotherapy, and gene therapy need to be further explored and researched.[7,8] Among these new therapies, phototherapy (photothermal therapy (PTT)/photodynamic therapy (PDT)) have the advantages of high specificity, low toxicity, and short treatment cycles.[9,10] Indocyanine green (ICG) is a new type of photosensitizer, which has excellent photothermal properties and is capable of effectively generating powerful reactive oxygen species (ROS). However, free ICG exhibits photodegradation, rapid blood clearance, and a low tumor accumulation rate.[11] Therefore, the selection of nanocarriers with higher biosafety and drug loading rates to load ICG can greatly improve its therapeutic effect on cancer.[12]

Owing to the complexity and heterogeneity of malignant tumors, a single novel therapy is unable to fully cover all tumor mutations and escape mechanisms, resulting in limited anti-tumor effects.[13] The current trend in research on novel tumor therapies has gradually shifted to combination therapies to achieve efficient tumor treatment.[14–16] Several studies have shown that combining phototherapy with other novel therapies has a significant anti-tumor effect and can effectively inhibit tumor recurrence and metastasis.[17] As a new type of anti-tumor therapy, chemodynamic therapy (CDT) can generate highly harmful reactive oxygen species through Fenton or Fenton-like reactions to induce apoptosis in tumor cells.[18,19]

https://doi.org/10.2147/IJN.S536173
Received: 16 May 2025
Accepted: 31 December 2025
Published: 18 January 2026

Graphical Abstract

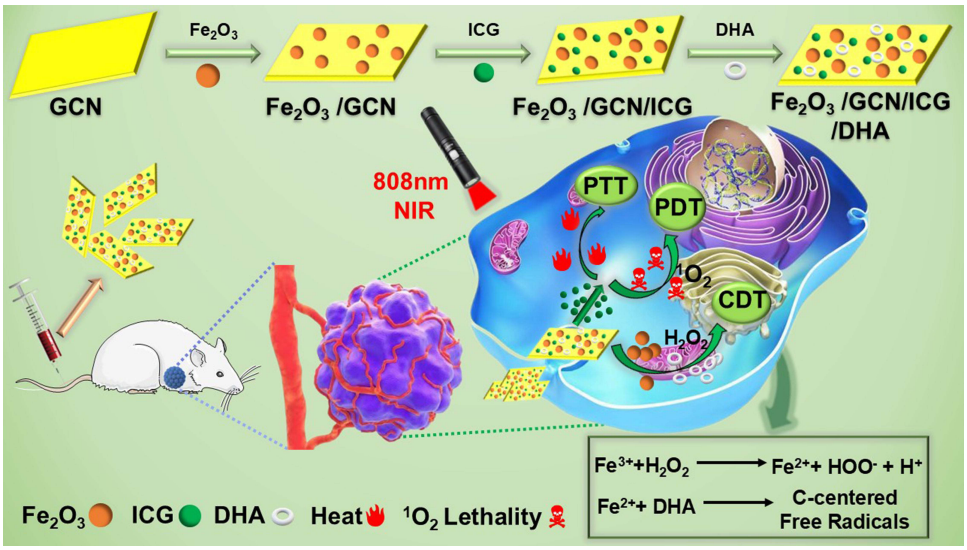

Dihydroartemisinin (DHA) is an anti-malarial drug extracted from *Artemisia annua* that has strong anti-tumor effects in vivo.[20] The peroxygen bonds in DHA can be cleaved by Fe^{2+} to generate C-centered free radicals, resulting in tumor cell damage and apoptosis.[21] However, the poor water solubility of DHA and the insufficient supply of Fe in solid tumors have limited its application in CDT. Therefore, it is essential to design nanomaterial-based drug delivery systems to improve the uptake efficiency of DHA and the concentration of iron ions at tumor sites.[22]

To address these problems, a simple and highly efficient transition metal iron-based nanocarrier containing DHA and ICG is designed and synthesized. This nanocarrier can increase the circulation time of ICG in the blood and the accumulation amount at the tumor site, as well as enhance the water solubility of DHA, etc. Currently, nanocarriers containing the transition metal Fe used in cancer therapy include metal sulfides, metal-organic frameworks, and carbon-based nanomaterials.[23–25] Carbon nitride (CN) has the advantages of rich surface functional groups, strong drug-carrying capacity, and good biocompatibility.[26] Therefore, carbon nitride has been widely used in the fields of biosensors, fluorescent labels, bioimaging, and drug delivery.[27–29] Lin et al demonstrated for the first time that GCN nanosheets could be used as effective photosensitizers and pH-responsive nanocarriers for cancer imaging and therapy.[30] Xia et al developed a donor-acceptor structure within a heterogeneous carbon nitride nanosheet and an interfacial heterostructure of copper-loaded metal molybdenum disulfide nanosheets (T-HGCN@CuMS), which exhibited excellent Fenton-like properties under near-infrared laser irradiation and achieved satisfactory results both in vitro and in vivo of anti-tumor and anti-metastasis effects.[31]

In this study, iron trioxide/carbon nitride nanosheets were prepared by high-temperature polymerization and in situ synthesis, and used as carriers to load ICG and DHA to construct Fe_2O_3/GCN/ICG/DHA nanocomplexes with PTT/PDT/CDT properties. Fe^{3+} in Fe_2O_3/GCN/ICG/DHA can be reduced to Fe^{2+} in the tumor microenvironment under high H_2O_2 conditions, and Fe^{2+} can react with DHA to generate C-center radicals to kill tumor cells. Moreover, ICG loaded on Fe_2O_3/GCN/ICG/DHA produced a warming effect and generated cytotoxic monoclinic oxygen under irradiation with an 808 nm laser. The results of Fe_2O_3/GCN/ICG/DHA in vitro and in vivo confirmed that Fe_2O_3/GCN/ICG/DHA has a higher efficient combined tumor treatment effect, providing a scientific basis for the application of novel nano-complex based on the transition metal Fe in the field of tumor therapy. Moreover, this work highlights the potential of Fe_2O_3 /GCN/ICG/DHA to tackle critical clinical hurdles like multidrug resistance and poor tumor selectivity, paving the way for novel nano-complexes in advanced cancer treatment.

Methods

Materials, Apparatus and Instrumentation

The detailed information of this part can be found in the Supporting Methods.

Preparation of Fe_2O_3/GCN/ICG/DHA

Carbon nitride nanosheets were prepared using a one-step thermal polymerization method.[32] Melamine (3.0 g) was ground using a mortar and pestle. The ground powder was placed in a muffle furnace, calcined at 520°C for 4 h, and cooled to room temperature to obtain bulk GCN. Bulk GCN (500 mg bulk GCN) was ground into powder and added to 200 mL of deionized water. The carbon nitride nanosheets were freeze-dried after ultrasonic treatment for 6 h (600 W) ultrasonic treatment.

The GCN nanosheets (0.6 g) and $FeCl_3 \cdot 6H_2O$ (0.2 g) were dissolved in anhydrous ethanol (20 mL) and stirred at room temperature for 0.5 h to obtain homogeneous mixtures. The stirred solution was dried at 60°C to obtain a light-yellow powder, which was then transferred to a covered crucible and placed in a muffle furnace at 350 °C for 2 h to obtain a brown powder. After the reaction product was dissolved in deionized water (15 mL), it was transferred to a PTFE reactor and heated at 160°C for 12 h. After cooling to room temperature, the reaction product was washed thoroughly with ethanol and deionized water to remove the unincorporated $FeCl_3$-$6H_2O$, and the precipitate was placed in an oven at 60°C for overnight to obtain Fe_2O_3/GCN.

10 mg Fe_2O_3/GCN was dissolved in 10 mL of methanol solution and sonicated for 30 min. ICG (3 mg) was weighed and dissolved in 10 mL of methanol solution, which was regarded as solution B. Solution B was added to solution A and stirred in the dark at 350 rpm for 12 h. The precipitate was collected by centrifugation at 10000 rpm for 15 min and washed several times with anhydrous ethanol and deionized water.[33] The washed products were dried overnight in an oven at 60°C to obtain the Fe_2O_3/GCN/ICG.

Dihydroartemisinin (4 mg) was dissolved in anhydrous ethanol (5 mL) and added to Fe_2O_3/GCN/ICG solution (10 mg, 10 mL). After stirring at room temperature for 24 h, free DHA was removed by alternate washing with anhydrous ethanol and deionized water. The Fe_2O_3/GCN/ICG/DHA powder was obtained after drying at 60°C overnight.

Determination of Drug Loading

DHA (5 mg) was dissolved in anhydrous ethanol (5 mL) to obtain the stock solution (1 mg/mL). Using a 0.2% NaOH solution as the solvent, the stock solution was diluted to 10, 20, 30, 40, 60, and 80 μg/mL standard solution to obtain a standard curve.

The weight ratio of DHA to Fe_2O_3/GCN/ICG was 1:1, 1:1.5, 1:2, 1:2.5, 1:3, and 1:3.5, respectively. After mixing the Fe_2O_3/GCN/ICG solution (10 mL, 1 mg/mL) with 10 mL DHA solutions of different concentrations for 24 h, the resulting reaction products were centrifuged at 10000 rpm for 15 min, and the products were alternately washed with anhydrous ethanol and deionized water. To measure DHA loading, the supernatants were collected and processed. The supernatant was mixed with 0.2% NaOH solution and heated at 55±1°C for 30 min. Subsequently, DHA in the supernatant was converted to a compound with characteristic ultraviolet absorption. The absorbance was measured at 288 nm using a UV-vis spectrophotometer. The drug-carrying capacity (DLC) of DHA was calculated using the following equation:[34]

$$DLC = \left(\frac{Initial\ Drug\ Quality - Supernatant\ Drug\ Quality}{Total\ mass\ of\ nanocomposites} \right) \times 100\%$$

Drug Release Studies

To study the drug release behavior of Fe_2O_3/GCN/ICG/DHA in different pH environments, Fe_2O_3/GCN/ICG/DHA (1 mg/mL, 5 mL) was dissolved in PBS (pH7.4, 5.5) and incubated at 37°C. After centrifugation at different time points (2, 4, 6, 8, 10, 12, and 24 h), the supernatant was mixed with 0.2% NaOH aqueous solution and heated at 55±1°C for

30 min to convert DHA into a UV-absorbing compound. The absorbance intensity at 288 nm was determined, and the rate of DHA release was calculated using the DHA standard curve.[35]

In vitro Photodynamic Performance Measurement

The DPBF probe was used to detect the photodynamic properties of Fe_2O_3/GCN/ICG/DHA in vitro by monitoring the singlet oxygen ($^1O_2$) generation.[36] The DPBF probe reacts with $^1O_2$, resulting in the weakening or disappearance of the characteristic absorption peak at 425 nm.

In vitro photodynamic experiments were divided into five groups: (1) DPBF, (2) DPBF+NIR, (3) DPBF+Fe_2O_3/GCN/ICG/DHA, (4) DPBF+Fe_2O_3/GCN/ICG+NIR, and (5) DPBF+Fe_2O_3/GCN/ICG/DHA+NIR. The concentrations of Fe_2O_3/GCN/ICG and Fe_2O_3/GCN/ICG/DHA were both 200 μg/mL, and a DPBF solution (1.2 mM) was prepared as the mother solution. The detailed treatment methods for each group were as follows: after mixing 2 mL of the material solution with 83 μL of DPBF, the material solution was irradiated with an 808 nm laser (1.8 W) for 10 min, and the absorbance values of the above solutions at 425 nm were measured using a UV-vis spectrophotometer every 2 min.

In vitro Chemical Dynamic Experiment

The DPBF probe was used to evaluate the ability of Fe^{2+} and DHA to generate C-centered free radicals.[37] The characteristic absorption peak of DPBF at 425 nm gradually decreases with the generation of C-center free radicals. The C-center free radical determination experiments were divided into the following five groups: (1) DHA, (2) Fe^{2+}, (3) DPBF+Fe^{2+}, (4) DPBF+DHA, and (5) DPBF+Fe^{2+}+DHA incubated at 37°C for 30 min. The absorbance at 425 nm was measured using a UV-vis spectrophotometer.

Cell Dark Toxicity Test

The MTT assay was used to evaluate the biocompatibility of the nanocomposites. The MCF-7 cell lines used were sourced from Shanghai Coweldgen Scientific Ltd (Shanghai, China). The cell lines of HUVEC was originated from the American Type Culture Collection (ATCC, Manassas, VA, USA). MCF-7 cells and HUVEC were seeded in 96-well plates for 24 h. After the cells were incubated with different concentrations of Fe_2O_3/GCN/ICG/DHA (0, 10, 20, 40, 60, 80, 120, 160, and 200 μg/mL) for 24 h, the supernatant was discarded, and the cells were rinsed with PBS to 2–3 times. 100 μL MTT (0.5 mg/mL) was then added to each well and incubated for 4 h. After rinsing the cells with PBS 2–3 times, 150 μL of DMSO solution was added. The absorbance at 490 nm was determined using an enzyme spectrometer, and the cell viability rate was calculated using the following equation:[38]

$$Cell\ Viability = \frac{A_{sample} - A_{blank}}{A_{control} - A_{blank}} \times 100\%$$

Cell Phototoxicity Test

MTT assay was used to evaluate the cytotoxicity of Fe_2O_3/GCN/ICG/DHA in vitro, which was divided into five groups: (1) GCN, (2) DHA, (3) Fe_2O_3/GCN/ICG/DHA+NIR, (4) Fe_2O_3/GCN/ICG/DHA+H_2O_2, and (5) Fe_2O_3/GCN/ICG/DHA+H_2O_2+NIR. MCF-7 cells were inoculated into 96-well plates and incubated for 24 h to allow them to adhere to cell walls. Different concentrations of GCN (0, 10, 20, 40, 60, 80, 120, 160, and 200 μg/mL), DHA (1, 1.3, 2.6, 5.2, 7.8, 10.4, 15.6, 20.8, and 26 μg/mL), and Fe_2O_3/GCN/ICG/DHA (0, 10, 20, 40, 60, 80, 120, 160, and 200 μg/mL) were used to incubate the cells for 24 h. Then, the supernatant was discarded, the cells were rinsed with PBS 2–3 times, and 150 μL DMSO was added. The absorbance of each well at 490 nm was determined using an enzyme-labeling apparatus, and the cell survival rate was calculated. Origin software was used to estimate IC50 values based on sigmoid concentration-response curve fitting models.

Cell Uptake Assay

The MCF-7 cells were inoculated into a laser confocal dish and incubated for 24 h to allow them to adhere to the wall. The cells were incubated with serum-free 1640 medium (1 mL) containing Fe_2O_3/GCN/ICG/DHA (100 μg/mL) for 4 h,

and the medium was discarded. After rinsing with PBS three times to remove the nanocomplexes, 1 mL of PBS was added, and cell intake images were collected using confocal laser microscopy at 405 and 640 nm.

Assay of Intracellular ROS

DCFH-DA probe was used to evaluate the ROS production of intracellular,[39] and the ROS determination experiments were divided into: (1) PBS group, (2) NIR group, (3) GCN group, (4) DHA group, (5) Fe_2O_3/GCN/ICG/DHA+H_2O_2 group, (6) Fe_2O_3/GCN/ICG/DHA+NIR group, and (7) Fe_2O_3/GCN/ICG/DHA+H_2O_2+NIR group. MCF-7 cells were inoculated into a confocal laser dish for 24 h with PBS, GCN (100 μg/mL), DHA (13 μg/mL), Fe_2O_3/GCN/ICG/DHA (100 μg/mL), Fe_2O_3/GCN/ICG/DHA (100 μg/mL), or H_2O_2 (250 mM). After incubation with serum-free 1640 medium for 4 h, cells were rinsed with PBS for 2–3 times. The cells were then incubated with the DCFH-DA probe (10 μM) for 30 min and rinsed with PBS 2–3 times. Cell images of different groups were captured using laser confocal microscopy at an excitation wavelength of 488 nm.[40]

Animals and Treatments

All animal experiment protocols were approved by the Medical Ethics Committee of Shanxi Medical University (2024pt11002). The protocols for animal experiments followed the Guidelines for the Use and Care of Experimental Animals at Shanxi Medical University. All animal studies were performed in compliance with relevant ethical regulations.

Female BALB/c mice (6-week, 20–25 g) purchased from SPF Biotechnology Co., Ltd. (Beijing, China) were used in the experiment. The cell lines of 4T1 was originated from the American Type Culture Collection (ATCC, Manassas, VA, USA). 4T1 cells were injected into the right underarm of the mice after shaving with a spatula to build a tumor-bearing mouse model. The mouse experiment was initiated when the tumor volume reached 100 mm^3.

Two mice with tumor volumes up to 100 mm^3 were selected and injected with Fe_2O_3/GCN/ICG/DHA solution (2 mg/mL, 100 μL) into the tail vein. Fluorescence images of the mice were collected at 0, 3, 6, 9, 12, and 24 h using a multimode imaging system. The distribution of Fe_2O_3/GCN/ICG/DHA in vivo. When the fluorescence accumulation was strongest at the tumor site, another mouse was sacrificed and dissected, and fluorescence images were collected from the major organs (heart, liver, spleen, lung, and kidney) and tumor tissues.

The photothermal imaging effect of the mice was recorded using an infrared thermal imager, and the tumor-bearing mice injected with normal saline, GCN, Fe_2O_3/GCN, Fe_2O_3/GCN-ICG, and Fe_2O_3/GCN/ICG/DHA solutions were irradiated with an 808 nm laser. Images were captured at different time points (0, 2, 4, 6, 8, and 10 min).

In total, 35 tumor-bearing mice with tumor volumes of approximately 100 mm^3 were randomly divided into seven groups (5 mice per group): (1) PBS, (2) NIR, (3) GCN, (4) DHA, (5) Fe_2O_3/GCN/ICG/DHA, (6) ICG+NIR, and (7) Fe_2O_3/GCN/ICG/DHA+NIR. At 0, 3, 6, 9, and 12 days, the mice in each group were injected via the tail vein (material concentration was 2 mg/mL, 100 μL), and the tumor site was irradiated by an 808 nm laser 9 h after intravenous injection (the light source was turned off for 5 min every 10 min after irradiation, and the irradiation was repeated three times at this time interval). The weight and tumor volume of the mice were recorded every two days.

The mice were sacrificed after 14 days of treatment, and orbital blood was collected for routine blood and biochemical index detection. Routine blood detection indicators include white blood cells (WBC), red blood cells (RBC), hematocrit (HCT), mean red blood cell volume (MCV), mean red blood cell hemoglobin (MCH), mean red blood cell hemoglobin concentration (MCHC), hemoglobin (HGB), and platelet count (HCT). The biochemical indicators included alanine aminotransferase (ALT), creatinine (CRE), urea nitrogen (BUN), aspartate aminotransferase (AST), total protein (TP), and albumin (ALB). HE staining was performed on the mouse tumors and heart, liver, spleen, lung, and kidney tissues.

Statistical Analysis

Statistical analysis was conducted using SPSS software. Data are presented as mean ± SD and were obtained from at least 3 independent experiments. Analysis of variance was used to assess the significance of differences between means. A p-value<0.05 indicated a statistically significant difference between the compared data.

Results and Discussion

Characterization of Fe2O3/GCN/ICG/DHA

The TEM image (Figure 1a) shows that the prepared GCN had a sheet-like structure. Well-dispersed Fe_2O_3 nanoparticles were synthesized on the surface of GCN nanoparticles using a hydrothermal method (Figure 1b). It can be seen from the inner illustration that Fe_2O_3 nanoparticles have obvious lattice stripes with a lattice spacing of 0.25 nm, corresponding to the (104) face of Fe_2O_3 NPs.[41] Figure 1c shows that ICG loading of ICG has no effect on the flaky structure of Fe_2O_3 /GCN,[42] and after the surface of Fe_2O_3/GCN/ICG was loaded with DHA (Figure 1d), the morphology of Fe_2O_3/GCN/ICG did not change.[18]

As shown in Figure 2a, Fe_2O_3/GCN/ICG/DHA consists of five elements: C, N, O, Fe, and S. Table S1 lists the relative contents of GCN, Fe_2O_3/GCN, Fe_2O_3/GCN/ICG, and Fe_2O_3/GCN/ICG/DHA. Figure 2b shows the fine spectrum of C1s in Fe_2O_3/GCN/ICG/DHA, where the peaks at 288.3 eV, 286.2 eV and 285 eV are attributed to O-C=O, C-O/C-N, and C=C/C-C bonds, respectively. The peaks at 398.7 eV, 399.5 eV, and 400.6 eV in Figure 2c are attributed to the C=N-C, N-(C_3), and C-N-H bonds, respectively. In the fine spectrum of O1s (Figure 2d), the peaks at 529.7 eV, 532, and 533.4 eV correspond to the O-Fe, C=O, and C-O bonds, respectively. As can be seen from Figure 2e, the Fe peaks at 711.15 eV and 724.5 eV belong to the 2p3/2 and 2p1/2 hybrid orbitals of Fe^{3+}, respectively.[43] The peaks of 167.8 eV and 163.6 eV in the fine spectrum of the S element are caused by the C-SOx-C and C-S bonds (Figure 2f). The above results indicate that the Fe_2O_3/GCN/ICG/DHA possesses a large number of functional groups, and the fitting spectrum of S confirm that ICG was successfully modified on the GCN. This once again demonstrates the successful preparation of the Fe_2O_3/GCN/ICG/DHA.

Figure 3a shows the ultraviolet absorption spectra of GCN, Fe_2O_3/GCN, Fe_2O_3/GCN/ICG, and Fe_2O_3/GCN/ICG/DHA. The characteristic absorption peak of GCN at 320 nm is caused by the n-π* transition of the lone pair of electrons on N atoms.[44] The Fe_2O_3 nanoparticles did not affect the characteristic UV absorption peak of the GCN. After ICG was introduced into Fe_2O_3/GCN/ICG, the characteristic UV absorption peak of ICG was redshifted from 785 to 820 nm. The redshift of the absorption peak may be caused by hydrophobic interactions between the aromatic ring of GCN and the benzene ring of ICG and π-π stacking.[45] A characteristic absorption peak of DHA (280 nm) was observed for Fe_2O_3 /GCN/ICG/DHA, which provided the basis for confirming the successful loading of DHA onto Fe_2O_3/GCN/ICG. At a maximum excitation wavelength of 320 nm, the maximum emission peak of GCN fluorescence was observed at 445 nm

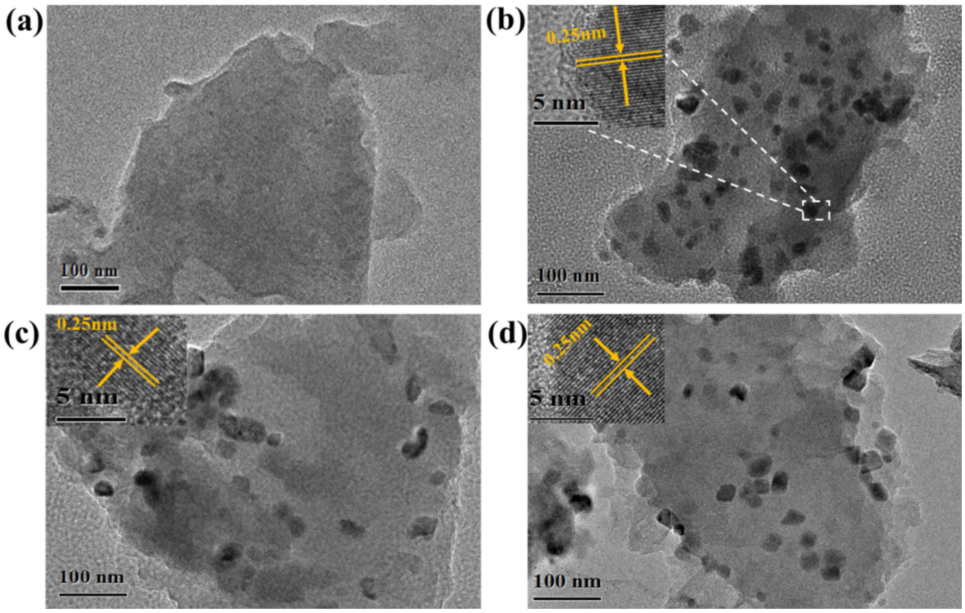

Figure 1 TEM images of (**a**) GCN, (**b**) Fe_2O_3/GCN, (**c**) Fe_2O_3/GCN/ICG, and (**d**) Fe_2O_3/GCN/ICG/DHA (inner illustration: HRTEM image of Fe_2O_3; the yellow lines, arrows and numbers are used to indicate the lattice spacing).

https://doi.org/10.2147/IJN.S536173

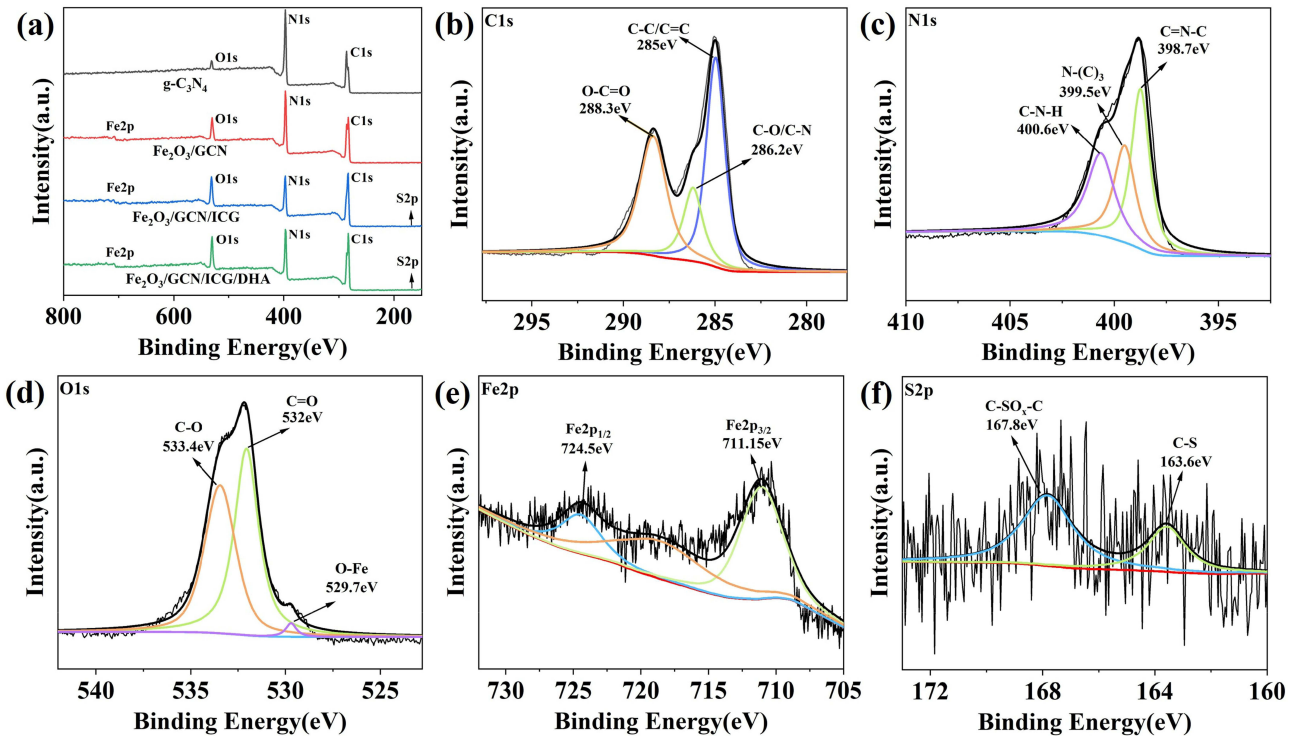

Figure 2 (**a**) Total XPS spectra of GCN, Fe_2O_3/GCN, Fe_2O_3/GCN/ICG, Fe_2O_3/GCN/ICG/DHA; Fine spectrum of Fe_2O_3/GCN/ICG/DHA (**b**) C1s, (**c**) N1s, (**d**) O1s, (**e**) Fe2p, (**f**) S2p.

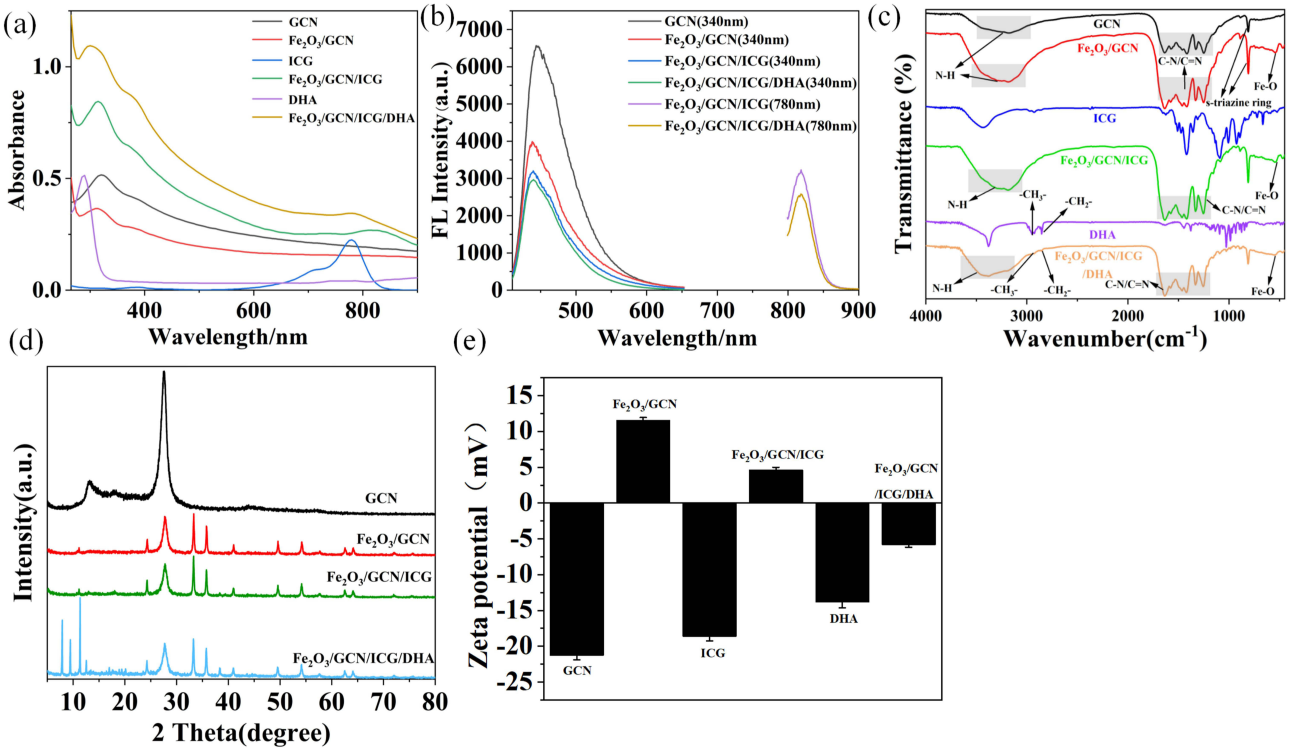

Figure 3 (**a**) UV-vis absorption, (**b**) Fluorescence, (**c**) FTIR spectra, (**d**) XRD patterns, and (**e**) Zeta potential diagram of GCN, Fe_2O_3/GCN, Fe_2O_3/GCN/ICG, and Fe_2O_3 /GCN/ICG/DHA.

https://doi.org/10.2147/IJN.S536173

(Figure 3b). It can be seen from the figure that Fe_2O_3/GCN and GCN have the same position of fluorescence emission peak, but the FL intensity is lower than that of GCN, which indicates that Fe_2O_3 weakens the recombination probability of photogenerated electrons and holes in GCN. At a maximum excitation wavelength of 780 nm, Fe_2O_3/GCN/ICG and Fe_2O_3/GCN/ICG/DHA showed a maximum emission peak at 814 nm, confirming that Fe_2O_3/GCN/ICG and Fe_2O_3/GCN/ICG/DHA could be used for fluorescence imaging.

The FT-IR spectra of GCN, Fe_2O_3/GCN, ICG, Fe_2O_3/GCN/ICG, DHA, and Fe_2O_3/GCN/ICG/DHA (Figure 3c) show that the wide absorption peak of GCN at 3000–3500 cm^{-1} is caused by the stretching vibration of the N-H bond. The region of 1200–1650 cm^{-1} is the stretching vibration peak of C-N and C=N, and the characteristic peak at 811 cm^{-1} corresponds to the bending vibration of the S-triazine ring.[46] Fe_2O_3/GCN had a stretching vibration peak attributed to the Fe-O bond at 532 cm^{-1}.[47–49] After modification with ICG, a new absorption peak appeared at 932 cm^{-1}, which was attributed to ICG. Compared with Fe_2O_3/GCN/ICG, Fe_2O_3/GCN/ICG/DHA has a new characteristic peak in the range of 900–1200 cm^{-1}, which is assigned to the tensile vibration peak of the O-O-C of the DHA molecule. The characteristic peaks of Fe_2O_3/GCN/ICG/DHA at 2850 cm^{-1} and 2940 cm^{-1} correspond to the tensile vibration peaks generated by methyl (-CH_3-) and ethyl (-CH_2-) groups in the molecular structure of DHA.[18,50] Characteristic diffraction peaks of 24.2°, 33.3°, 35.7°, 41.0°, 49.6°, 54.2°, 57.7°, 62.5°, 64.1° and 72.1° appear in the XRD pattern of Fe_2O_3/GCN (Figure 3d), corresponding to the (012), (104), (110), (113), (124), (116), (018), (214), (300) and (1010) crystal faces of Fe_2O_3.[51] The characteristic diffraction peaks of GCN also exist in the XRD pattern of Fe_2O_3/GCN, confirming the successful formation of the Fe_2O_3/GCN nanosheets. After ICG and DHA modification, typical diffraction peaks of Fe_2O_3 and GCN were still observed in the Fe_2O_3/GCN/ICG/DHA spectrum, confirming that ICG and DHA did not affect the crystal structure of Fe_2O_3/GCN.

It can be seen from Figure 3e that the Zeta potential of GCN and Fe_2O_3/GCN is −21.26 mV and 11.56 mV, respectively, which is due to the reduction of the surface charge of GCN after introduce the Fe_2O_3 NPs with positively charged.[52] Owing to the negative charge of ICG, the potential of Fe_2O_3/GCN loaded with ICG was 4.62 mV, and the potential of Fe_2O_3/GCN/ICG/DHA was −5.8 mV after the introduction of negatively charged DHA. These results demonstrate that Fe_2O_3/GCN/ICG/DHA was successfully prepared.

Determination of Drug Loading and Release

Drug loading refers to the amount of drug loaded per unit weight of the nanocomplex and is used to evaluate the drug-loading capacity of the nanocomplex. When the drug-loading ratio was 2.5:1, the maximum drug-loading ratio was 21.23% (Figure S1), confirming that Fe_2O_3/GCN/ICG has the potential to be used as a drug carrier. Compared with existing works, the drug loading rate of this work is much higher than that of other nanomaterials.[53,54] Therefore, an optimal drug-loading ratio of 2.5:1 was used for subsequent experiments.

As shown in Figure S2, the drug release rate of Fe_2O_3/GCN/ICG/DHA in PBS (pH 7.4) was 12.61%, while that in PBS (pH 5.5) reached 52.92%, indicating that Fe_2O_3/GCN/ICG/DHA has pH-responsive drug release properties. Similarly, the DHA release rate in this study is much higher than that of other nanomaterials reported previously.[54,55]

In vitro Photodynamic Performance Measurement

The absorbance of DPBF, DPBF+NIR, and DPBF+Fe_2O_3/GCN/ICG/DHA remained unchanged. After irradiation by 808 nm laser, the absorbance of DPBF+Fe_2O_3/GCN/ICG/DHA+NIR and DPBF+Fe_2O_3/GCN/ICG/DHA+NIR gradually decreased with the increase of irradiation time (Figure 4). It was confirmed that Fe_2O_3/GCN/ICG can produce $^1O_2$ under laser irradiation, and that DHA loading does not affect the photodynamic properties of Fe_2O_3/GCN/ICG/DHA, which provides a basis for subsequent PDT at the cellular and animal levels.

Photothermal Properties in vitro

To evaluate the photothermal properties of Fe_2O_3/GCN/ICG/DHA in vitro, an 808 nm laser was used as the light source. First, the photothermal capabilities of different groups of solutions under a fixed laser power (1.8 W) were investigated (Figure 5a). The solution temperature of H_2O, GCN, and Fe_2O_3/GCN did not increase significantly after 10 min of irradiation by the 808 nm laser, while the solution temperature of the Fe_2O_3/GCN/ICG and Fe_2O_3/GCN/ICG/DHA groups increased to

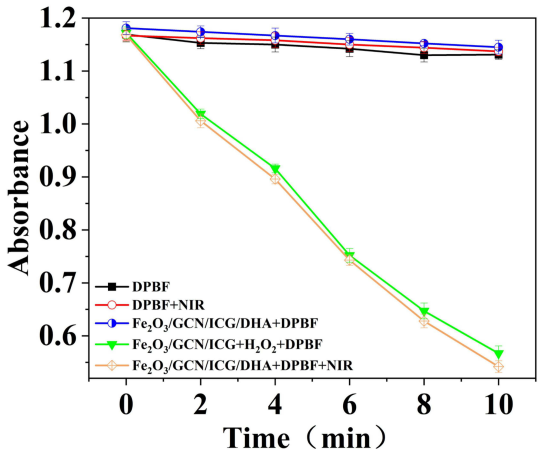

Figure 4 UV absorption intensity of DPBF at 450 nm for different groups over time (n = 3).

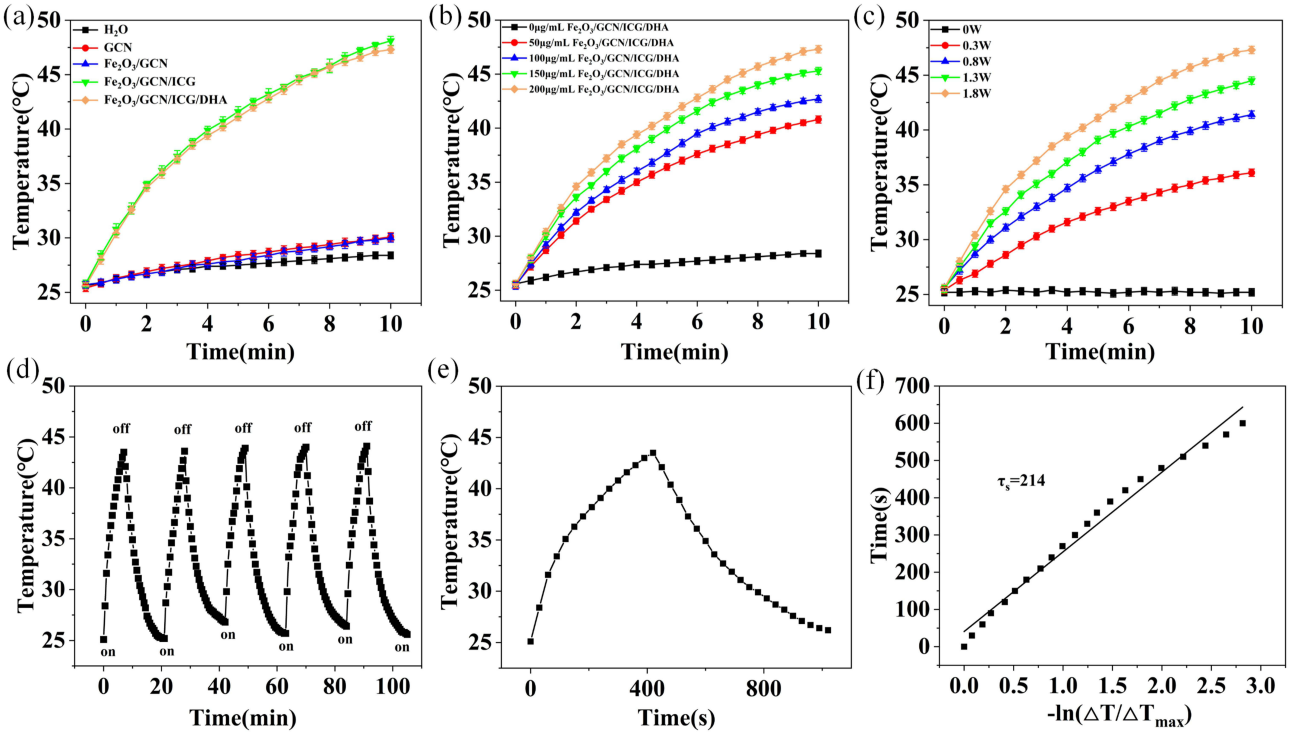

Figure 5 (**a**) Photothermal conversions of different groups under 808 nm laser (1.8 (W) (n = 3), (**b**) Photothermal conversions of Fe_2O_3/GCN/ICG/DHA with various concentrations under 808 nm laser (1.8 (W) (n = 3), (**c**) Photothermal conversions of Fe_2O_3/GCN/ICG/DHA with various laser power under 808 nm laser (n = 3), (**d**) Temperature of Fe_2O_3/GCN/ICG/DHA during five on/off cycles upon the 808 nm laser irradiation, (**e**) The temperature of Fe_2O_3/GCN/ICG/DHA dispersion during the 808 nm laser irradiation for 400 s and the 808 nm laser shutdown for 600 s, (**f**) Linear relationship between the time after the 808 nm laser shutdown and -ln(θ) obtained from the cooling period of (**f**) (ΔT and ΔT_{max} means the change of temperature and the max change of temperature).

48.1°C and 47.3°C, respectively. Compared with the Au-based photothermal nanomaterials, although the temperature rise of the Fe_2O_3/GCN/ICG/DHA does not exceed 50°C, this mild treatment can effectively avoid damage to the surrounding tissues of the tumor. With an increase in the concentration and laser light power, the heating effect of Fe_2O_3/GCN/ICG/DHA improved (Figure 5b and c). Figure 5d shows the temperature change of Fe_2O_3/GCN/ICG/DHA by periodically turning the laser source on and off. Thus, it can be concluded that Fe_2O_3/GCN/ICG/DHA had good photothermal stability.

https://doi.org/10.2147/IJN.S536173

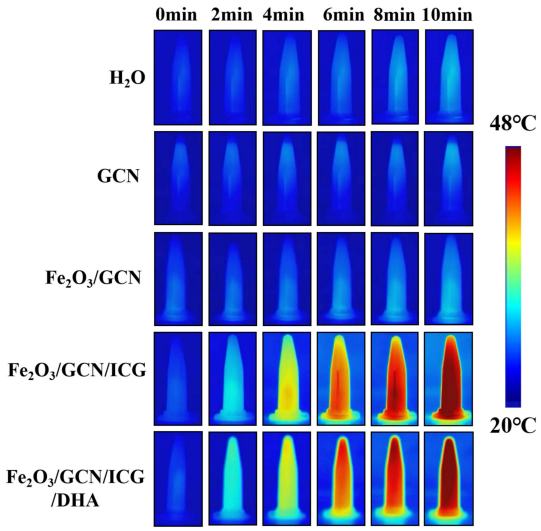

Figure 6 Time dependent infrared thermal imaging of H_2O, GCN, Fe_2O_3/GCN, Fe_2O_3/GCN/ICG, Fe_2O_3/GCN/ICG/DHA under laser (808 nm, 1.8 (W) irradiation for 10 min.

In addition, the photothermal efficiency (η) of Fe_2O_3/GCN/ICG/DHA nanocomposite was calculated (Supporting Methods). Figure 5e shows the heating and cooling curves of Fe_2O_3/GCN/ICG/DHA, and Figure 5f shows the linear relationship between cooling time and ln(θ). Based on the calculation shown as $t = -\tau_S ln\theta$, the value of τ_S is determined to be 214. Derived from the detailed calculation formula (1) and (2), the η is quantified at 31.43%. Compared with other works, the η of Fe_2O_3/GCN/ICG/DHA is much higher than that of other nanomaterials.[56,57] Figure 6 shows the photothermal imaging of each group of solution with 808 nm laser irradiation (1.8 W, 10 min). The color of the H_2O, GCN, and Fe_2O_3 /GCN groups did not change significantly after 10 min of laser irradiation. The Fe_2O_3/GCN/ICG and Fe_2O_3/GCN/ICG/DHA groups showed obvious color changes that gradually deepened, indicating that the Fe_2O_3/GCN/ICG/DHA group has good photothermal imaging ability in vitro. These results confirmed that Fe_2O_3/GCN/ICG/DHA had good photothermal properties.

$$\eta = \frac{hS(T_{max} - T_{surr}) - Q_{dis}}{I\left(1 - 10^{-A}\right)} \tag{1}$$

$$hS = \frac{mC_{water}}{\tau_S} \tag{2}$$

In vitro Chemical Dynamic Experiment

As shown in Figure S3, the DPBF solution exhibited a strong absorption peak at 420 nm, and the absorbance of DPBF remained unchanged when Fe^{2+} or DHA was incubated with DPBF alone. In contrast, after DPBF was incubated with DHA and Fe^{2+} simultaneously, the absorbance of DPBF decreased significantly within 10 min, indicating that the joint action of DHA and Fe^{2+} can generate C-centered free radicals that can exert chemical dynamic effects. In addition, with increasing incubation time, the DPBF absorbance showed a decreasing trend.

Cellular Experiment

Cell Dark Toxicity Test

The standard MTT method was used to determine the toxicity of Fe_2O_3/GCN/ICG/DHA in MCF-7 cells and HUVEC. As shown in Figure S4, after incubating the cells with Fe_2O_3/GCN/ICG/DHA at a concentration of 0–200 μg/mL for 24 h, the cell survival rate of MCF-7 and HUVEC remained above 80%, indicating that Fe_2O_3/GCN/ICG/DHA had good cellular biocompatibility.

Cell Phototoxicity Test

To assess the phototoxicity of Fe_2O_3/GCN/ICG/DHA in MCF-7 cells, the cells were incubated with different concentrations of the materials (0–200 μg/mL). It can be seen from the Figure S5 that the cell survival rate of GCN and DHA remained above 90% after incubation with materials for 24 h. But, the cells treated with Fe_2O_3/GCN/ICG/DHA+NIR, Fe_2O_3/GCN/ICG/DHA+H_2O_2, Fe_2O_3/GCN/ICG/DHA+NIR+H_2O_2, and rate was significantly decreased to different degrees. The cell survival rates in the Fe_2O_3/GCN/ICG/DHA+NIR and Fe_2O_3/GCN/ICG/DHA+H_2O_2 groups were 45.71% and 55.99%, respectively. The combination treatment group (Fe_2O_3/GCN/ICG/DHA+NIR+H_2O_2) showed the highest cytotoxicity with a cell survival rate of only 22.74%, which was significantly different from the survival rates of the cells treated by other groups. The recorded IC50 value for Fe_2O_3/GCN/ICG/DHA+H_2O_2 against the growth of MCF-7 is 256.1 μg/mL, respectively. Fe_2O_3/GCN/ICG/DHA+NIR recorded IC50 value of 185.0 μg/mL for MCF-7 cells. However, Fe_2O_3/GCN/ICG/DHA+NIR+H_2O_2 recorded an IC50 value of 53.14 μg/mL. The above results indicate that the effect of a single component (GCN and DHA) in killing cells is negligible. However, when laser and H_2O_2 are present, the killing effect of Fe_2O_3/GCN/ICG/DHA on cells is quite obvious.

Cell Uptake Assay

Figure 7 shows the uptake of Fe_2O_3/GCN/ICG/DHA by MCF-7 cells based on the blue fluorescence of GCN (405 nm) and the red fluorescence of ICG (640 nm). Compared to the control group (PBS), MCF-7 cells treated with Fe_2O_3/GCN/ICG/DHA emitted blue and red fluorescence, indicating that Fe_2O_3/GCN/ICG/DHA was successfully taken up by MCF-7 cells through endocytosis.

Assay of Intracellular ROS

The intracellular ROS levels were measured using a DCFH-DA probe. As Figure 8a, the PBS, NIR, GCN, and DHA groups did not produce obvious green fluorescence signals. The green fluorescence signals in the Fe_2O_3/GCN/ICG/DHA+H_2O_2 and Fe_2O_3/GCN/ICG/DHA+NIR groups were attributed to the formation of C-center free radicals by Fe^{2+} and DHA and the $^1O_2$ produced by ICG under 808 nm laser irradiation, respectively. These results indicate that Fe_2O_3/GCN/ICG/DHA can generate $^1O_2$ in cells. After cells incubated with Fe_2O_3/GCN/ICG/DHA+H_2O_2 under laser irradiated, the intracellular green fluorescence signal was significantly higher than that of Fe_2O_3/GCN/ICG/DHA+ H_2O_2 and Fe_2O_3/GCN/ICG/DHA+NIR groups, which is result of the interaction between $^1O_2$ and the C-center radical. Furthermore, the fluorescence intensities of each group of cells are quantified (Figure 8b), allowing for a more intuitive understanding of the ability of each group to produce ROS. Based on the above results, the following conclusion

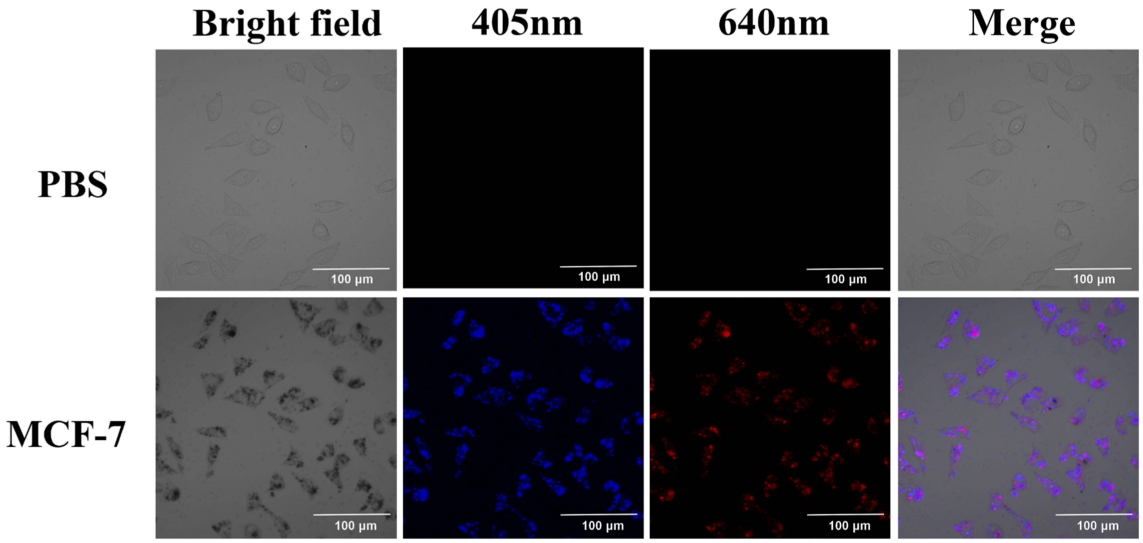

Figure 7 Fluorescence imaging of MCF-7 cells incubated with Fe_2O_3/GCN/ICG/DHA (100 μg/mL), The first panels are bright field images. The second and third fourth panels are cell images taken at 405 nm and 640 nm, respectively. The fourth panels were combined with the first, second, and third, panels. Scale bar: 100 μm.

https://doi.org/10.2147/IJN.S536173

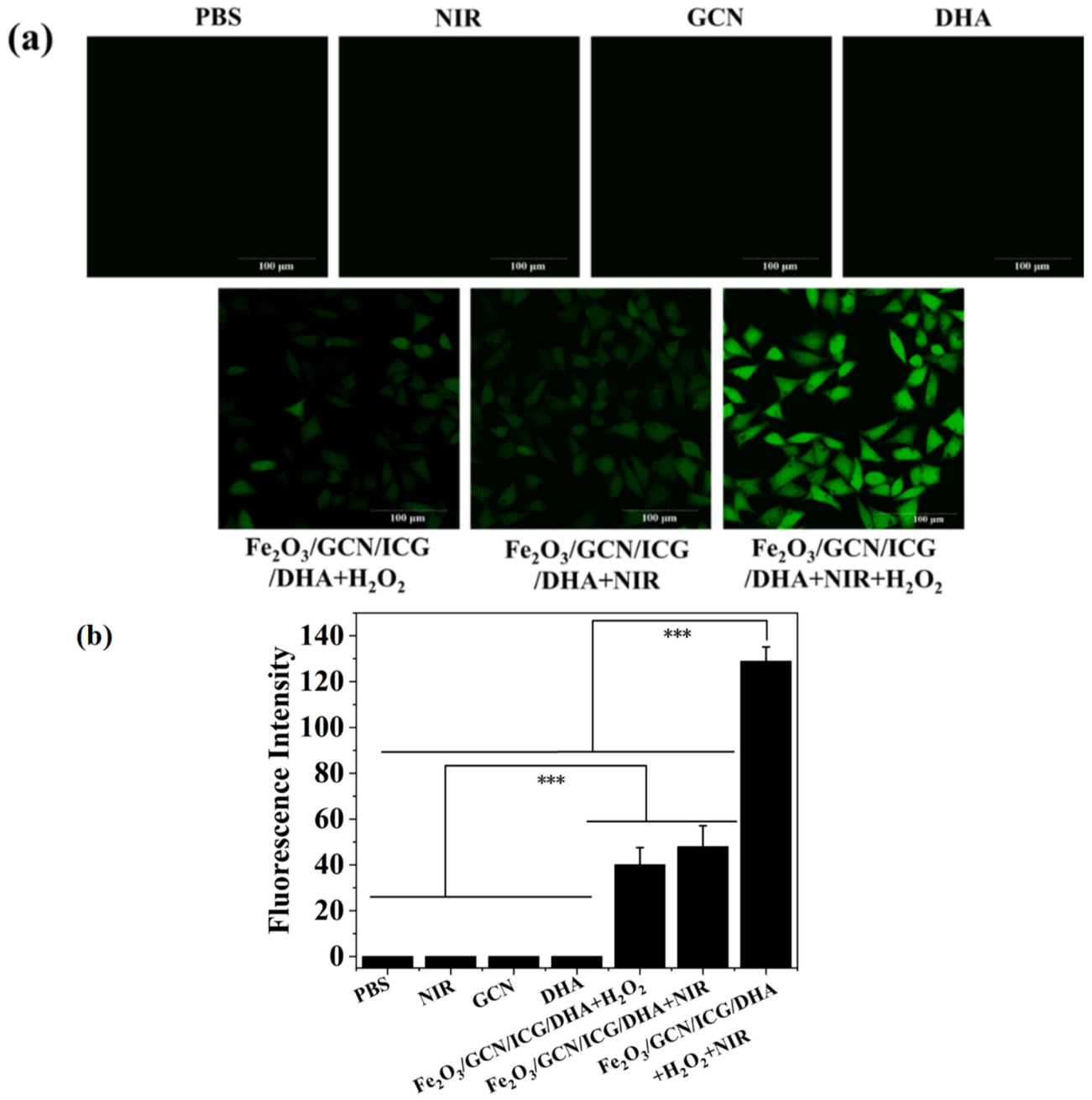

Figure 8 (**a**) ROS production in PBS, NIR, GCN, DHA, Fe_2O_3/GCN/ICG/DHA+H_2O_2, Fe_2O_3/GCN/ICG/DHA+NIR and Fe_2O_3/GCN/ICG/DHA+ H_2O_2+NIR group after incubation of MCF-7 cells for 30 min. (**b**) Analysis of cell fluorescence intensity in each group (***p<0.001).

can be drawn: When both laser and H_2O_2 are present, the amount of ROS produced by the Fe_2O_3/GCN/ICG/DHA is much higher than that of either single component or a single treatment group. From this, we can conclude that the Fe_2O_3 /GCN/ICG/DHA can achieve a synergistic therapeutic effect.

AM/PI Double Staining of Living and Dead Cells

The CALCIN-AM/PI live and dead cell double staining kit can be used for double staining and labeling of living and dead cells. Dead cells show red fluorescence, and live cells show green fluorescence, which can be used to visually monitor cell survival. The details can be found in the Supporting Methods. Figure 9 shows the survival of MCF-7 cells after incubation with different materials. Cells treated with PBS, NIR, GCN, or DHA exhibited whole-field green

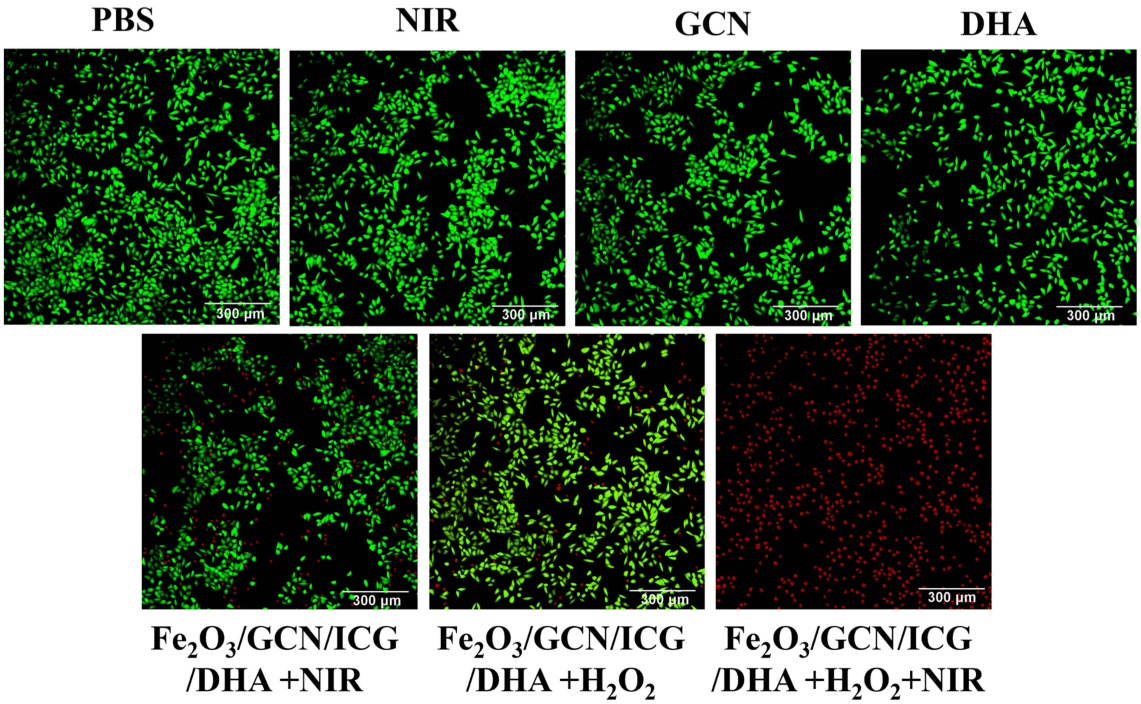

Figure 9 Therapeutic effection of PBS, NIR, GCN, DHA, Fe_2O_3/GCN/ICG/DHA+H_2O_2, Fe_2O_3/GCN/ICG/DHA+NIR group on MCF-7 cells, Scale bar: 300 μm.

fluorescence signals, indicating no cell death. In the Fe_2O_3/GCN/ICG/DHA+H_2O_2 and Fe_2O_3/GCN/ICG/DHA+NIR groups, red and green fluorescence signals were observed simultaneously. The red fluorescence signal of the Fe_2O_3 /GCN/ICG/DHA+H_2O_2 group was higher than that of the Fe_2O_3/GCN/ICG/DHA+NIR group, indicating that the tumor-killing effect of the PDT/PTT group was better than that of the CDT group. In the combined treatment group, the red fluorescence signal of the whole field indicated that the tumor cells were apoptotic. These results indicate that Fe_2O_3 /GCN/ICG/DHA combination therapy can effectively induce apoptosis in tumor cells. The quantitative analysis of the live and dead cells viability can more intuitively demonstrate the above results (Figure S6).

Apoptosis Test

Flow cytometry was used to evaluate the therapeutic effect of Fe_2O_3/GCN/ICG/DHA on the tumors. The details can be found in the Supporting Methods. As shown in Figure 10a, the apoptosis rates in the PBS, NIR, GCN, and DHA groups were lower than 10%. The apoptosis rates in the Fe_2O_3/GCN/ICG/DHA+H_2O_2, Fe_2O_3/GCN/ICG/DHA+NIR, and Fe_2O_3 /GCN/ICG/DHA+H_2O_2+NIR groups were 46.6, 33.87, and 75.77%, respectively. Furthermore, the apoptosis rates of each group are quantitatively summarized (Figure 10b), allowing for a more intuitive understanding of the apoptosis status of each group of cells. The results showed that Fe_2O_3/GCN/ICG/DHA could effectively induce apoptosis in tumor cells and had a good anti-tumor effect.

Evaluation of Anti-Tumor Effect in vivo

Mice Fluorescence Imaging

The distribution and behavior of Fe_2O_3/GCN/ICG/DHA in tumor-bearing mice were studied using a multimodal small-animal imaging system. As Figure 11a, the FL intensity at the tumor site of tumor-bearing mice gradually increased and reached a maximum 9 h post-injection. At 24 h post-injection, the fluorescence signal of the tumor site was significantly decreased, whereas that of the liver region was enhanced, indicating that Fe_2O_3/GCN/ICG/DHA was mainly metabolized by the liver. Figures 11b and S7 show the fluorescence images and quantitative analysis of the major organs and tumor tissues of mice treated with Fe_2O_3/GCN/ICG/DHA at 9 h post-injection. There were obvious fluorescence signals in the tumor tissue, indicating that Fe_2O_3/GCN/ICG/DHA accumulated at the tumor site 9 h post-injection. This may be due to

https://doi.org/10.2147/IJN.S536173

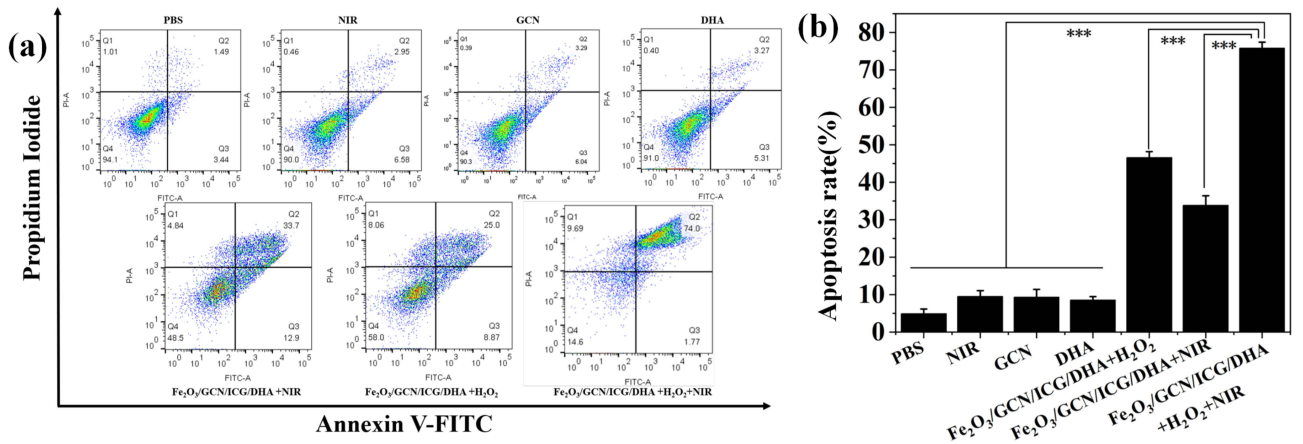

Figure 10 (**a**) Cell apoptosis and (**b**) apoptosis rate of MCF-7 cells treated with PBS, NIR, GCN, DHA, Fe_2O_3/GCN/ICG/DHA+H_2O_2, Fe_2O_3/GCN/ICG/DHA+H_2O_2+NIR and Fe_2O_3/GCN/ICG/DHA+H_2O_2+NIR (***p<0.001).

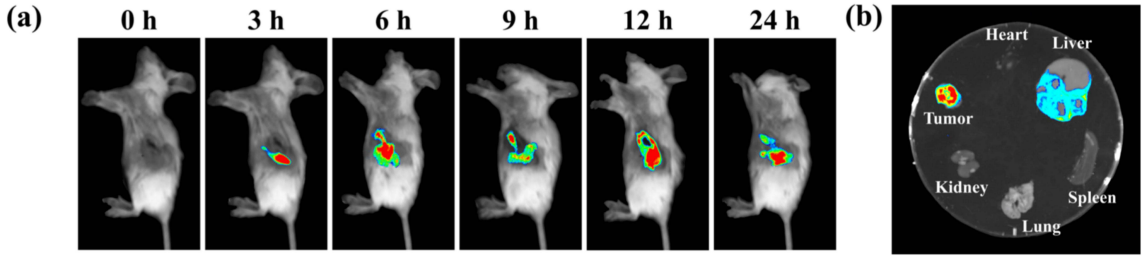

Figure 11 (**a**) Fluorescence images of mouse treated with Fe_2O_3/GCN/ICG/DHA at different time points (0, 3, 6, 9, 12, and 24 h). (**b**) Fluorescence images of major organs (heart, liver, spleen, kidney, and lung) and tumor in Fe_2O_3/GCN/ICG/DHA-treat mice.

the fact that Fe_2O_3/GCN/ICG/DHA is more likely to penetrate into tumor tissues and remain for a long time compared with normal tissues. Although Fe_2O_3/GCN/ICG/DHA has a good accumulation at the tumor site, it takes too long for it to be excreted from the body. Further in-depth research can be conducted on this work in the future.

Photothermal Imaging of Mice

The photothermal imaging effect of tumor-bearing mice was recorded using an infrared thermal imager. As shown in Figure 12, the temperature of the tumor sites in the mice treated with normal saline, GCN, and Fe_2O_3/GCN did not change after 10 min of laser irradiation. However, the tumors of mice treated with Fe_2O_3/GCN/ICG and Fe_2O_3/GCN/ICG/DHA showed an obvious warming trend with increasing irradiation time, and the tumor site temperature of the Fe_2O_3/GCN/ICG/DHA group could reach 46.9°C after irradiation for 10 min. These results indicate that Fe_2O_3/GCN/ICG/DHA can effectively accumulate at the tumor site in mice and has a good photothermal imaging effect in vivo.

Tumor Treatment in vivo

The body weight of the mice in each group remained unchanged during treatment (Figure 13a), which indirectly indicated that the Fe_2O_3/GCN/ICG/DHA nanocomposite had no obvious toxic side effects in mice. As shown in Figure 13b and c, at the end of the treatment cycle, the tumor volumes in the saline, NIR, GCN, and DHA groups were 9.1, 8.9, 8.6 and 8.7 times that those at the start of treatment, and the mean tumor weight were 1.76 g, 1.78 g, 1.69 g and 1.81 g, respectively. The tumor volume and the average tumor weight of ICG+NIR and Fe_2O_3/GCN/ICG/DHA groups increased to 3.5 times and 0.59 g, and 4.7 times and 0.68 g, respectively, indicating that PTT/PDT therapy and CDT therapy could inhibit tumor growth to a certain extent. The tumor volume of Fe_2O_3/GCN/ICG/DHA+NIR group was reduced to about 2/3 of the initial volume, and the average tumor weight was 0.24 g, which was significantly lower than the above six groups. As shown in Figure 13d and e, at the end of treatment, the tumors in the combined treatment

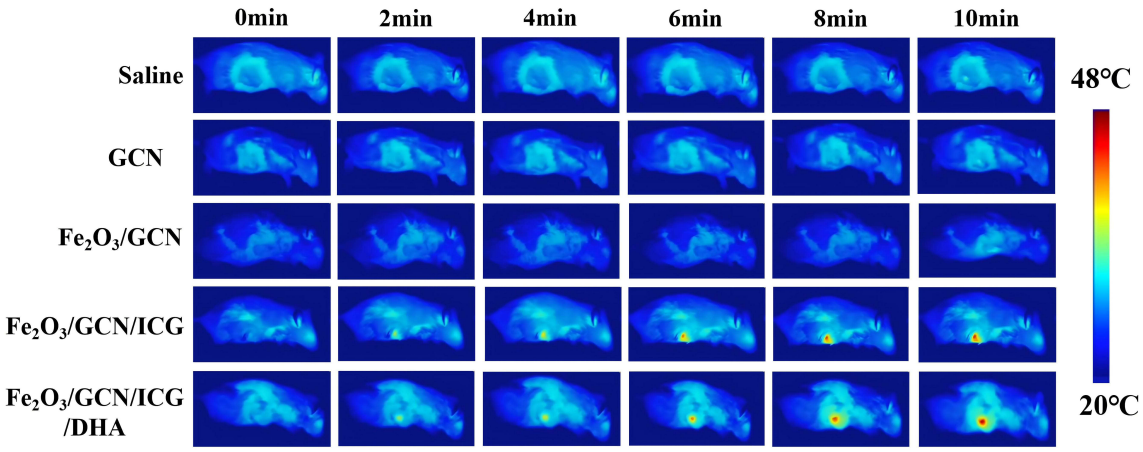

Figure 12 Infrared thermal imaging images of tumor-bearing mice with different treatments.

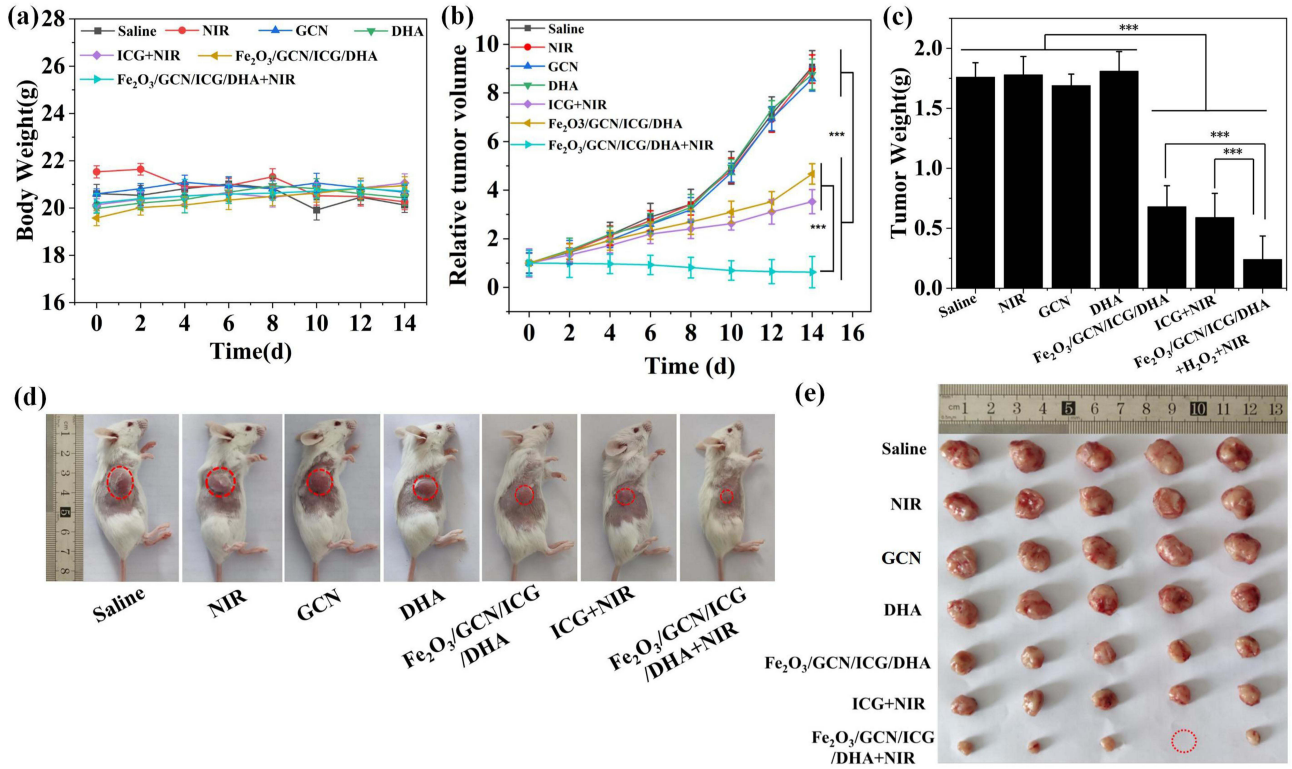

Figure 13 (**a**) Weight changes, (**b**) relative tumor volume, (**c**) tumor weight, (**d**) pictures of different groups of mice, (**e**) tumor tissue pictures of tumor-bearing mice after different treatments (***$p<0.001$). The red circle in (**d**) marks the location of the tumor. In figure (**e**), it shows that after the treatment, the tumor has completely disappeared in this mouse.

group were significantly smaller than those in the other groups. These results indicate that Fe_2O_3/GCN/ICG/DHA combination therapy has a significant anti-tumor effect.

Biosafety

Routine blood and biochemical indicators were determined after the mice were euthanized following treatment. Routine blood tests included RBC, WBC, PLT, HGB, HCT, MCV, MCHC, and MCH and biochemical indicators including ALB/TP, AST/ALT, and CRE/UREA. As shown in Figure S8, there was no significant difference between the indices of mice in the treatment group and those in the control group, and all indices were within the normal range, which confirmed that

https://doi.org/10.2147/IJN.S536173

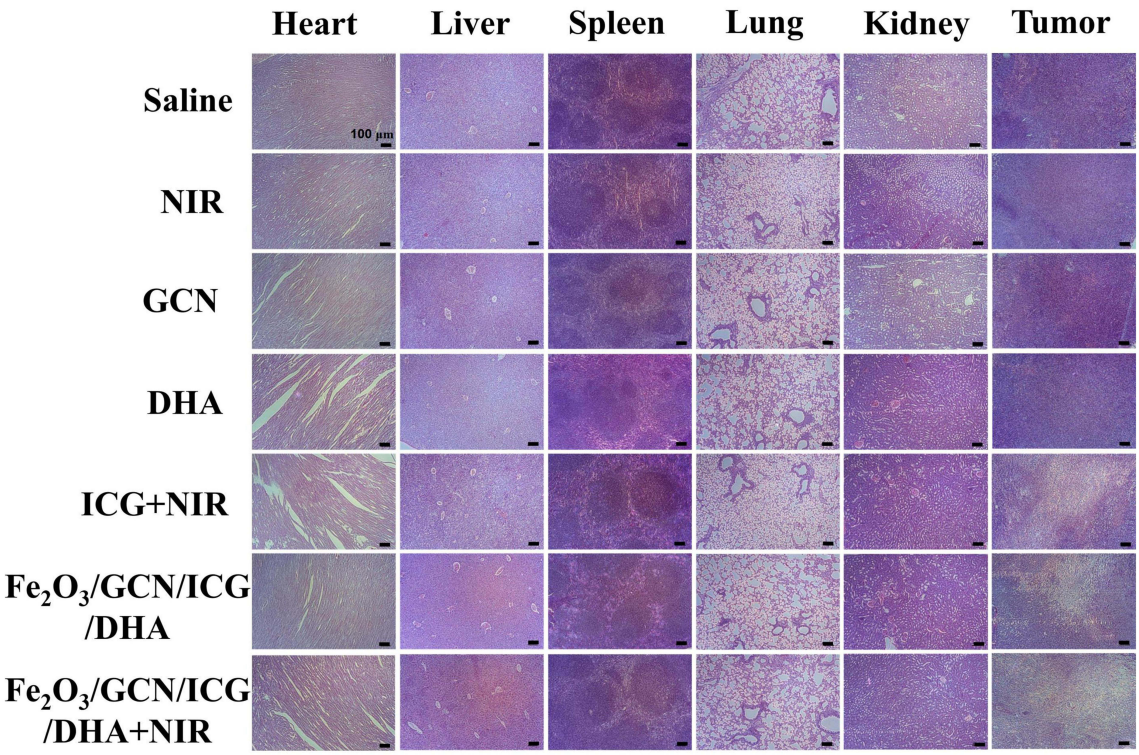

Figure 14 HE staining of normal tissues (heart, liver, spleen, lung, and kidney) and tumor tissues of mice in each group (100 μm scale).

Fe_2O_3/GCN/ICG/DHA did not cause inflammation or abnormal liver and kidney function in mice. HE staining of mouse tissues (Figure 14) showed no significant pathological changes in the major organs of the heart, liver, spleen, lung, and kidney, indicating that the material did not damage normal organs in mice. Compared with the results of HE staining in the tumor tissues of the control group, it can be seen that the tumor tissues of the single treatment group showed obvious ablation, and the tumor tissues of the combined treatment group showed a large area ablation, indicating that Fe_2O_3 /GCN/ICG/DHA had a significant anti-tumor effect under near-infrared laser irradiation.

Conclusion

In this study, GCN was synthesized by a high-temperature calcination method, Fe_2O_3/GCN was prepared as the carrier, and the photosensitizer ICG and drug DHA were loaded on the surface to construct Fe_2O_3/GCN/ICG/DHA, which was applied in the combined treatment of tumors. In vitro experiments showed that Fe_2O_3/GCN/ICG/DHA can produce $^1O_2$ and has a temperature rise under 808 nm laser irradiation, which has photodynamic and photothermal properties. Fe_2O_3 /GCN/ICG/DHA could selectively enter tumor cells and produce $^1O_2$, resulting in the apoptosis of tumor cells through PTT/PDT/CDT combination therapy. Compared with a single type of nanomaterial, the results of the in vivo experiments indicate that the Fe_2O_3/GCN/ICG/DHA drug combination can effectively inhibit the growth of tumor cells in mice, and its biocompatibility. However, there are still some issues that require further in-depth research, such as the relatively long time it takes for Fe_2O_3/GCN/ICG/DHA to be excreted from the body or its relatively low photothermal performance. Furthermore, in the subsequent research, the focus will be on analyzing apoptotic markers, thereby exploring the mode of cell death. In summary, we constructed a carbon nitride-based Fe_2O_3/GCN/ICG/DHA for photothermal/photodynamic/chemodynamic multi-effect combined therapy of tumors, thereby expanding the application of carbon nitride in bio-nanomedicine.

Ethics Statement

The animal study protocol was approved by the Medical Ethics Committee of Shanxi Medical University (Approval No. 2024pt11002), all experiments were conducted in strict accordance with the institutional Guidelines for the Use and Care of Experimental Animals at Shanxi Medical University with every effort made to minimize animal suffering; all cell lines used in this study were obtained from commercial sources, specifically, the 4T1 and HUVEC cell lines were purchased from the American Type Culture Collection (ATCC, Manassas, VA, USA), and the MCF-7 cell line was obtained from Shanghai Coweldgen Scientific Ltd (Shanghai, China).

Acknowledgments

This work was supported by the Central Guidance Fund for Science and Technology Development (YDZJSX2024C028, YDZJSX2025D061), the Natural Science Foundation of Shanxi Province of China (202203021221186&201901D111210), the Science and technology innovation projects of Shanxi Provincial University (2025L028) and the Shanxi Province Higher Education "Billion Project" Science and Technology Guidance Project (BYJL025).

Disclosure

The authors report no conflicts of interest in this work.

References

1. Li X, Shen M, Yang J, et al. Pillararene-based stimuli-responsive supramolecular delivery systems for cancer therapy. *Adv Mater*. 2024;36(16):2313317. doi:10.1002/adma.202313317
2. Cheng C, Wang H, Zhao J, et al. Advances in the application of metal oxide nanozymes in tumor detection and treatment. *Colloids Surf B*. 2024;235:113767. doi:10.1016/j.colsurfb.2024.113767
3. Domka W, Bartusik-Aebisher D, Rudy I, et al. Photodynamic therapy in brain cancer: mechanisms, clinical and preclinical studies and therapeutic challenges. *Front Chem*. 2023;11:1250621. doi:10.3389/fchem.2023.1250621
4. Silva JP, Pinto B, Monteiro L, et al. Combination therapy as a promising way to fight oral cancer. *Pharmaceutics*. 2023;15(6):1653. doi:10.3390/pharmaceutics15061653
5. Dongsar TT, Dongsar TS, Abourehab M, et al. Emerging application of magnetic nanoparticles for breast cancer therapy. *Eur Polym J*. 2023;187:111898. doi:10.1016/j.eurpolymj.2023.111898
6. Wang L, C D, Jiang B, et al. Adjusting the dose of traditional drugs combined with immunotherapy: reshaping the immune microenvironment in lung cancer. *Front Immunol*. 2023;14:1256740. doi:10.3389/fimmu.2023.1256740
7. Tai Y, Chen Z, Luo T, et al. MOF@COF Nanocapsules enhance soft tissue sarcoma treatment: synergistic effects of photodynamic therapy and PARP inhibition on tumor growth suppression and immune response activation. *Adv Healthcare Mater*. 2024;13(11):2303911. doi:10.1002/adhm.202303911
8. Wang X, Liu J, Yn LD, et al. Recent updates on the efficacy of mitocans in photo/radio-therapy for targeting metabolism in chemo/radio-resistant cancers: nanotherapeutics. *Curr Med Chem*. 2025;32(11):2156–2182. doi:10.2174/0109298673259347231019121757
9. Zhang F, Chen J, Luo W, et al. Mitochondria targeted biomimetic platform for chemo/photodynamic combination therapy against osteosarcoma. *Int J Pharm*. 2024;652:123865. doi:10.1016/j.ijpharm.2024.123865
10. Yang JK, Kwon H, Kim S. Recent advances in light-triggered cancer immunotherapy. *J Mat Chem B*. 2024;12(11):2650–2669. doi:10.1039/D3TB02842A
11. Zhang J, Zhang K, Hao Y, et al. Polydopamine nanomotors loaded indocyanine green and ferric ion for photothermal and photodynamic synergistic therapy of tumor. *J Colloid Interface Sci*. 2023;633:679–690. doi:10.1016/j.jcis.2022.11.099
12. Chen Y, Wang B, Chen W, et al. Co-delivery of dihydroartemisinin and indocyanine green by metal-organic framework-based vehicles for combination treatment of hepatic carcinoma. *Pharmaceutics*. 2022;14(10):2047. doi:10.3390/pharmaceutics14102047
13. Liu J, Liu H, Huang S, et al. Multiple treatment of triple-negative breast cancer through gambogic acid-loaded mesoporous polydopamine. *Small*. 2024;20(31):2309583. doi:10.1002/smll.202309583
14. Qin W, Qiao L, Wang Q, et al. Advancing precision: a controllable self-synergistic nanoplatform initiating pyroptosis-based immunogenic cell death cascade for targeted tumor therapy. *ACS Nano*. 2024;18(2):1582–1598. doi:10.1021/acsnano.3c09499
15. Miao YB, Ren HX, Zhang G, et al. Achieving precise non-invasive ROS spatiotemporal manipulation for colon cancer immunotherapy. *Chem Eng J*. 2024;481:148520. doi:10.1016/j.cej.2024.148520
16. Das B. Transition Metal complex-loaded nanosystems: advances in stimuli-responsive cancer therapies. *Small*. 2025;21(7):2410338. doi:10.1002/smll.202410338
17. Li Y, Qi H, Geng Y, et al. Research progress of organic photothermal agents delivery and synergistic therapy systems. *Colloids Surf B*. 2024;234:113743. doi:10.1016/j.colsurfb.2024.113743
18. Yang XX, Xu X, Wang MF, et al. A nanoreactor boosts chemodynamic therapy and ferroptosis for synergistic cancer therapy using molecular amplifier dihydroartemisinin. *J Nanobiotechnol*. 2022;20(1):230. doi:10.1186/s12951-022-01455-0
19. Shao L, Hu T, Fan X, et al. Intelligent nanoplatform with multi therapeutic modalities for synergistic cancer therapy. *ACS Appl Mater Interfaces*. 2022;14(11):13122–13135. doi:10.1021/acsami.2c01913

20. Rani K, Sahu RC, Chaudhuri A, et al. Exploring combinations of dihydroartemisinin for cancer therapy: a comprehensive review. *Biochem Biophys Res Commun*. 2025;765:151854. doi:10.1016/j.bbrc.2025.151854
21. Zhang Y, Chen B, Wei P, et al. Single-atom nanozyme-mediated dihydroartemisinin delivery for self-enhanced chemodynamic therapy and ferroptosis. *Mater Today Bio*. 2025;34:102096. doi:10.1016/j.mtbio.2025.102096
22. Yu Z, Luo X, Zhang C, et al. Mitochondria-targeted carrier-free nanoparticles based on dihydroartemisinin against hepatocellular carcinoma. *Chin Chem Lett*. 2024;35(10):109519. doi:10.1016/j.cclet.2024.109519
23. Chen J, Hu S, Sun M, et al. Recent advances and clinical translation of liposomal delivery systems in cancer therapy. *Eur J Pharm Sci*. 2024;193:106688. doi:10.1016/j.ejps.2023.106688
24. Duan S, Hu Y, Zhao Y, et al. Nanomaterials for photothermal cancer therapy. *RSC Adv*. 2023;13(21):14443–14460. doi:10.1039/D3RA02620E
25. Ni K, Lan G, Song Y, et al. Biomimetic nanoscale metal–organic framework harnesses hypoxia for effective cancer radiotherapy and immunotherapy. *Chem Sci*. 2020;11(29):7641–7653. doi:10.1039/D0SC01949F
26. Sathya V, Santhoshkumar S, Thirunavukkarasu S, et al. Amplifying anticancer and DNA fragmentation activities through surface-functionalization of nanorods-like graphitic carbon nitride sheets. *Diamond Relat Mater*. 2025;155:112252. doi:10.1016/j.diamond.2025.112252
27. Palani G, Apsari R, Hanafiah MM, et al. Metal-doped graphitic carbon nitride nanomaterials for photocatalytic environmental applications—a review. *Nanomaterials*. 2022;12(10):1754. doi:10.3390/nano12101754
28. Zeng X, Hou M, Zhu P, et al. g-C_3N_5-dots as fluorescence probes prepared by an alkali-assisted hydrothermal method for cell imaging. *RSC Adv*. 2022;12(41):26476–26484. doi:10.1039/D2RA03934F
29. Li M, Xiao M, Pan Q, et al. Multifunctional nanoplatform based on g-C_3N_4, loaded with MnO_2 and CuS nanoparticals for oxygen self-generation photodynamic/photothermal synergistic therapy. *Photodiagn Photodyn Ther*. 2022;37:102684. doi:10.1016/j.pdpdt.2021.102684
30. Lin LS, Cong ZX, Li J, et al. Graphitic-phase C_3N_4 nanosheets as efficient photosensitizers and pH-responsive drug nanocarriers for cancer imaging and therapy. *J Mat Chem B*. 2014;2(8):1031–1037. doi:10.1039/c3tb21479f
31. Xia J, Hu C, Ji Y, et al. Copper-loaded nanoheterojunction enables superb orthotopic osteosarcoma therapy via oxidative stress and cell cuproptosis. *ACS Nano*. 2023;17(21):21134–21152. doi:10.1021/acsnano.3c04903
32. Li Z, Bai H, Wei J, et al. One-step synthesis of melamine-sponge functionalized carbon nitride for excellent water sterilization via photogenerated holes and photothermal conversion. *J Colloid Interface Sci*. 2022;610:893–904. doi:10.1016/j.jcis.2021.11.126
33. Hou M, Ye M, Liu L, et al. Azide-locked prodrug Co-assembly into nanoparticles with indocyanine green for chemophotothermal therapy. *Mol Pharmaceut*. 2022;19(9):3279–3287. doi:10.1021/acs.molpharmaceut.2c00452
34. Yu W, Wang Q, Liu Z, et al. Metal-phenolic network crosslinked nanogel with prolonged biofilm retention for dihydroartemisinin/NIR synergistically enhanced chemodynamic therapy. *J Colloid Interface Sci*. 2025;678:841–853. doi:10.1016/j.jcis.2024.09.168
35. Yang C, Ming H, Li B, et al. A pH and glutathione-responsive carbon monoxide-driven nano-herb delivery system for enhanced immunotherapy in colorectal cancer. *J Control Release*. 2024;376:659–677. doi:10.1016/j.jconrel.2024.10.043
36. Qi C, Tan G, Hu H, et al. Prussian blue-decorated indocyanine green-loaded mesoporous silica nanohybrid for synergistic photothermal-photodynamic-chemodynamic therapy against methicillin-resistant Staphylococcus aureus. *Colloids Surf B*. 2024;241:114065. doi:10.1016/j.colsurfb.2024.114065
37. Feng G, Huang H, Zhang M, et al. Single atom iron-doped graphic-phase C_3N_4 semiconductor nanosheets for augmented sonodynamic melanoma therapy synergy with endowed chemodynamic effect. *Adv Sci*. 2023;10(23):2302579. doi:10.1002/advs.202302579
38. Duarte D, Falcão SI, El Mehdi I, et al. Honeybee venom synergistically enhances the cytotoxic effect of CNS drugs in HT-29 colon and MCF-7 breast cancer cell lines. *Pharmaceutics*. 2022;14(3):511. doi:10.3390/pharmaceutics14030511
39. Xia Y, Liu C, Zhao X, et al. Highly stable and near-infrared responsive phase change materials for targeted enzyme delivery toward cancer therapy. *Mater Today Bio*. 2024;29:101345. doi:10.1016/j.mtbio.2024.101345
40. Pan Q, Xie L, Zhu H, et al. Curcumin-incorporated EGCG-based nano-antioxidants alleviate colon and kidney inflammation via antioxidant and anti-inflammatory therapy. *Regen Biomater*. 2024;11:rbae122. doi:10.1093/rb/rbae122
41. Kheradmand A, Wainwright A, Wang L, et al. Anchoring iron oxides on carbon nitride nanotubes for improved photocatalytic hydrogen production. *Energy Fuels*. 2020;35(1):868–876. doi:10.1021/acs.energyfuels.0c03901
42. Miao W, Shim G, Kim G, et al. Image-guided synergistic photothermal therapy using photoresponsive imaging agent-loaded graphene-based nanosheets. *J Control Release*. 2015;211:28–36. doi:10.1016/j.jconrel.2015.05.280
43. Ding Q, Lam FLY, Hu X. Complete degradation of ciprofloxacin over g-C_3N_4-iron oxide composite via heterogeneous dark Fenton reaction. *J Environ Manage*. 2019;244:23–32. doi:10.1016/j.jenvman.2019.05.035
44. Zhao G, Li B, Yang X, et al. Two birds with one stone: engineering polymeric carbon nitride with n-π^* electronic transition for extending light absorption and reducing charge recombination. *Adv Powder Mater*. 2023;2(1):100077. doi:10.1016/j.apmate.2022.100077
45. Liu C, Chen J, Zhu Y, et al. Highly sensitive MoS_2–indocyanine green hybrid for photoacoustic imaging of orthotopic brain glioma at deep site. *Nano-Micro Lett*. 2018;10(3):48. doi:10.1007/s40820-018-0202-8
46. Shang Q, Zhang L, Chen C, et al. Fe_3O_4/g-C_3N_4 nanozyme for production of L-DOPA as mimetics of tyrosine hydroxylase. *ChemNanoMat*. 2023;9(2):e202200409. doi:10.1002/cnma.202200409
47. Khasim S, Pasha A, Dastager SG, et al. Design and development of multi-functional graphitic carbon nitride heterostructures embedded with copper and iron oxide nanoparticles as versatile sensing platforms for environmental and agricultural applications. *Ceram Int*. 2023;49(12):20688–20698. doi:10.1016/j.ceramint.2023.03.200
48. Khalil KD, Bashal AH, Habeeb T, et al. Multifunctional lanthanum oxide-doped carboxymethyl cellulose nanocomposites: a promising approach for antimicrobial and targeted anticancer applications. *Int J Biol Macromol*. 2024;283:137495. doi:10.1016/j.ijbiomac.2024.137495
49. Saddik MS, Elsayed MM, El-Mokhtar MA, et al. Tailoring of novel azithromycin-loaded zinc oxide nanoparticles for wound healing. *Pharmaceutics*. 2022;14(1):111. doi:10.3390/pharmaceutics14010111
50. Saddik MS, Al-Hakkani MF, Abu-Dief AM, et al. Formulation and evaluation of azithromycin-loaded silver nanoparticles for the treatment of infected wounds. *Int J Pharm*. 2024;7:100245.
51. Mani G, Nair PR, Mathew S. Polymeric carbon nitride/iron oxide composites: a novel class of catalysts with reduced metal content for ammonium perchlorate thermal decomposition. *ACS omega*. 2022;7(43):38512–38524. doi:10.1021/acsomega.2c03761

52. Ikhaylov VI, Torlopov MA, Krivoshapkina EF, et al. Heteroaggregation of cellulose nanocrystals with Fe_2O_3 nanoparticles. *J Sol Gel Sci Techn*. 2017;88(1):6–12. doi:10.1007/s10971-017-4374-3
53. Gu X, Cheng Q, He P, et al. Dihydroartemisinin-loaded chitosan nanoparticles inhibit the rifampicin-resistant mycobacterium tuberculosis by disrupting the cell wall. *Front Microbiol*. 2021;12:735166. doi:10.3389/fmicb.2021.735166
54. Wu Y, He Y, Pan X, et al. Encapsulation of dihydroartemisinin with tannic acid/Fe coated hollow mesoporous silica nanoparticles for tumor therapy. *Mater Today Commun*. 2024;38:107951. doi:10.1016/j.mtcomm.2023.107951
55. Lu J, Yu J, Xie W, et al. Acidity-triggered charge-convertible conjugated polymer for dihydroartemisinin delivery and tumor-specific Chemo-Photothermal therapy. *ACS Appl Bio Mater*. 2023;6(6):2303–2313. doi:10.1021/acsabm.3c00169
56. Cao Y, Wen E, Chen Q, et al. Multifunctional ICG-SB@Lip-ZA nanosystem focuses on remodeling the inflammatory-immunosuppressive microenvironment after photothermal therapy to potentiate cancer photothermal immunotherapy. *Adv Healthcare Mater*. 2025;14(1):2402211. doi:10.1002/adhm.202402211
57. Zhang W, Chen L, Cui M, et al. Successively triggered rod-shaped protocells for enhanced tumor chemo-photothermal therapy. *Eur J Pharm Biopharm*. 2021;169:1–11. doi:10.1016/j.ejpb.2021.08.012